



## **Observation of magnetic islands in tokamak plasmas during the suppression of edge-localized modes**

Downloaded from: <https://research.chalmers.se>, 2026-04-16 05:43 UTC

Citation for the original published paper (version of record):

Mitterauer, V., Hoelzl, M., Suttrop, W. et al (2024). Observation of magnetic islands in tokamak plasmas during the suppression of edge-localized modes. *Nature Physics*, 20(12): 1980-1988. <http://dx.doi.org/10.1038/s41567-024-02666-y>

N.B. When citing this work, cite the original published paper.

# Observation of magnetic islands in tokamak plasmas during the suppression of edge-localized modes

Received: 31 August 2023

Accepted: 13 September 2024

Published online: 28 October 2024

 Check for updates

Matthias Willensdorfer<sup>1</sup>✉, Verena Mitterauer<sup>1</sup>, Matthias Hoelzl<sup>1</sup>, Wolfgang Suttrop<sup>1</sup>, Mark Cianciosa<sup>2</sup>, Mike Dunne<sup>1</sup>, Rainer Fischer<sup>1</sup>, Nils Leuthold<sup>3</sup>, Jonas Puchmayr<sup>1</sup>, Oleg Samoylov<sup>1</sup>, Guillermo Suárez López<sup>4</sup>, Daniel Wendler<sup>1,5</sup> & the ASDEX Upgrade Team\*

In tokamaks, a leading platform for fusion energy, periodic filamentary plasma eruptions known as edge-localized modes occur in plasmas with high-energy confinement and steep pressure profiles at the plasma edge. These edge-localized modes could damage the tokamak wall but can be suppressed using small three-dimensional magnetic perturbations. Here we demonstrate that these magnetic perturbations can change the magnetic topology just inside the steep gradient region of the plasma edge. We identify signatures of a magnetic island, and their observation is linked to the suppression of edge-localized modes. We compare high-resolution measurements of perturbed magnetic surfaces with predictions from ideal magnetohydrodynamic theory where the magnetic topology is preserved. Although ideal magnetohydrodynamics adequately describes the measurements in plasmas exhibiting edge-localized modes, it proves insufficient for plasmas where these modes are suppressed. Nonlinear resistive magnetohydrodynamic modelling supports this observation. Our study experimentally confirms the predicted role of magnetic islands in inhibiting the occurrence of edge-localized modes. This will be beneficial for physics-based predictions in future fusion devices to control these modes.

To achieve an economically viable fusion power plant based on the tokamak concept<sup>1</sup>, it will be necessary to operate in plasma scenarios with good energy confinement such as the high confinement mode (H-mode)<sup>2</sup>. The reason for the high confinement in H-mode is the large pressure gradient at the plasma edge, which produces a pressure ‘pedestal’ and enhances the core pressure. These steep pressure profiles make the plasma edge prone to magnetohydrodynamic (MHD) instabilities causing filamentary eruptions of particles and energy called edge-localized modes (ELMs)<sup>3</sup>. According to recent scaling studies based on data from multiple tokamaks<sup>4</sup>, the particle and energy content

of ELM filaments will damage plasma-facing components in future fusion devices, placing an additional constraint on tokamak fusion power plants. They will have to operate with good energy confinement and without ELMs<sup>5</sup>.

Small three-dimensional (3D) perturbations of the plasma surface referred to as resonant magnetic perturbations (RMPs) are a highly effective method<sup>6</sup> to control ELMs while sustaining a sufficiently high plasma confinement. They are generated by additional ‘saddle’ coils and distort the toroidal symmetry (axisymmetry) of the tokamak plasma. Their capability to completely suppress ELMs has

<sup>1</sup>Max Planck Institute for Plasma Physics, Garching, Germany. <sup>2</sup>Oak Ridge National Laboratory, Oak Ridge, TN, USA. <sup>3</sup>Columbia University, New York, NY, USA. <sup>4</sup>ITER Organization, Saint-Paul-lès-Durance, France. <sup>5</sup>Physics Department, TUM School of Natural Sciences, Technical University of Munich, Garching, Germany. \*A list of authors and their affiliations appears at the end of the paper. ✉e-mail: [matthias.willensdorfer@ipp.mpg.de](mailto:matthias.willensdorfer@ipp.mpg.de)

been successfully demonstrated in multiple tokamaks<sup>6–9</sup>. The possibility of using the RMP coil currents to actively control ELMs, while simultaneously optimizing the energy confinement<sup>10</sup>, makes RMPs an attractive tool for future tokamaks<sup>11,12</sup>. However, understanding the physics mechanism behind ELM suppression by RMPs is crucial to make accurate predictions.

Rational magnetic surfaces are of particular importance for understanding the response of the plasma to RMPs. These surfaces are exceptional because they exhibit magnetic field lines that close on themselves after an integral number of toroidal and poloidal turns<sup>13</sup>. Rational surfaces are susceptible to small magnetic perturbations that are aligned to the magnetic field. In the presence of finite plasma resistivity, magnetic field lines can reconnect, which alters the topology of magnetic surfaces and can form magnetic islands inside the plasma. In the tokamak edge where neighbouring rational surfaces are located very close to each other, magnetic islands can even overlap and induce a stochastic magnetic field topology.

Early explanations for ELM suppression suggested that RMPs penetrate the plasma edge and induce a stochastic magnetic field topology, which causes enhanced outward transport of plasma particles and heat. The reduced pressure gradient in the pedestal region avoids the ELM instability<sup>6</sup>. This explanation is contradicted by experimental observations in H-mode, in which changes in particle transport are primarily observed. Stochastic transport theory, however, would mainly enhance the electron heat transport and lower the electron temperature ( $T_e$ )<sup>6</sup>. In addition, MHD theory and the generalized Ohm's law<sup>14</sup> predict helical screening currents on rational surfaces that shield the plasma from magnetic perturbations and prevent a stochastic magnetic field topology. These screening currents depend on the flow velocity of the electron fluid and are especially prominent in the H-mode pedestal, where steep pressure gradients drive a strong flow. Penetration of RMPs is, therefore, more likely in plasma regions with low pressure gradients.

Although RMPs are screened in the H-mode pedestal, they can still have a notable impact on the magnetic surface geometry of the plasma edge. Because of the steep pressure gradient and accompanied current densities, small magnetic perturbations can result in a considerable kinking of the plasma boundary. These kink modes are well described by ideal MHD theory where the plasma is assumed to be an ideal conductor and the magnetic topology is preserved. They are marginally stable and can even amplify the externally applied perturbations, which is well documented in refs. 15–19.

One prominent hypothesis for ELM suppression suggests that penetration of RMPs in H-mode is still possible just inside the steep gradient region at the top of the pedestal<sup>20</sup>, where the pressure gradient and, thus, the electron fluid velocity becomes small. It is proposed that RMPs excite ideal kink modes, which can even amplify the perturbation<sup>8,21,22</sup>. Their perturbations extend further inside the gradient region and drive the formation of a magnetic island at a rational surface at the top<sup>23–26</sup>. The associated transport limits the radial extension of the edge pressure pedestal. According to a predictive pedestal model called EPED<sup>20</sup>, this constraint on the pedestal width is then sufficient to prevent the occurrence of ELMs.

The magnetic island hypothesis explains well (1) the observed windows in ELM suppression when the positions of the rational surfaces at the pedestal top are scanned<sup>27,28</sup>, (2) the empirically observed importance of coupling between the ideal kink modes and edge rational surfaces<sup>8,9,21</sup> and (3) the sudden changes in magnetic probe measurements during the transition from plasmas with ELMs (ELMy plasmas) to ELM-suppressed plasmas<sup>7,29</sup>. While a flattening of kinetic profiles (such as the  $T_e$  profile) at the pedestal top is commonly observed during the transition to ELM-suppressed plasmas<sup>23,30</sup>, a connection to a magnetic island remains unconfirmed. The observed flattening could also originate from an island with a different toroidal mode number (for example,  $n = 1$  instead of  $n = 2$ ) or additional turbulent transport without the need for an island<sup>31</sup>. Previous attempts to identify helical

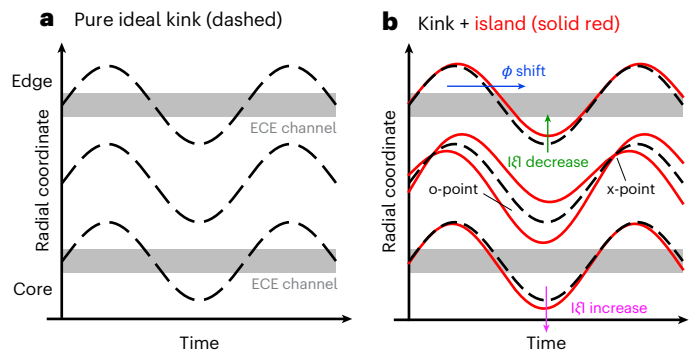


**Fig. 1 | Challenge of measuring magnetic islands in kinking plasmas. a, b.** The cartoon illustrates local measurements of rotating perturbed magnetic surfaces (lines) or constant electron temperature ( $T_e$ ) contours. While magnetic surface perturbations from pure ideal kink modes (dashed lines) are easily measured by  $T_e$  perturbations using the local ECE (grey bars) (a), an additional small magnetic island with its o-point and x-point (solid red line) might only be visible by small changes in the magnetic surface displacement amplitude  $|\xi|$  and in its phase  $\phi$  with respect to the pure ideal kink mode (b). Panel b adapted with permission from ref. 50 under a Creative Commons license CC BY 4.0.

perturbations in  $T_e$  from a potential magnetic island using jumps in the toroidal phase of the applied RMP field were inconclusive in experiments compensating the intrinsic error field<sup>24,32</sup>.

Here, we present observations of a magnetic island at the pedestal top in ELM-suppressed plasmas in the Axial Symmetric Divertor EXperiment Upgrade (ASDEX-Upgrade) tokamak. This is achieved by comparing ideal MHD predictions with measurements of the internal magnetic topology using  $T_e$  (ref. 33) in ELM-suppressed plasmas and in plasmas with ELMs.

## Measuring magnetic islands

To identify changes in the magnetic topology such as the formation of magnetic islands,  $T_e$  is the best plasma parameter owing to the fast electron heat transport parallel to the magnetic field lines<sup>34</sup>. Since  $T_e$  is practically constant along a field line and, hence, on a magnetic surface, a short-circuit of magnetic field lines by a magnetic island appears predominantly in  $T_e$ . Spectrally resolved intensity measurements of the electron cyclotron emission (ECE) allows the determination of high temporal and spatial resolution  $T_e$  profiles<sup>35</sup> in regions where the plasma behaves as a black body radiator (Extended Data Figs. 1 and 2). ECE is, therefore, commonly used to identify rotating magnetic islands from measured  $T_e$  perturbations<sup>36</sup>. However, small magnetic islands are still difficult to measure because of the competition between parallel heat transport around the island and the perpendicular transport across the island. To cause measurable  $T_e$  perturbations, the island size has to exceed a critical island width ( $W_{crit}$ )<sup>34</sup>, above which the parallel heat transport around the island begins to dominate<sup>34</sup>.

Because of its magnetic topology, a rotating magnetic island is usually identified by a  $\pi$ -phase jump in the measured  $T_e$  perturbation around the island<sup>36</sup>. This typical change in phase may not be seen in the case of ELM suppression by RMPs because the possible magnetic island is accompanied by dominating ideal kink modes<sup>37</sup>. Moreover, both have the same toroidal mode number and are phase locked to the RMP field. To probe such a magnetic island using measurements at a single toroidal location, one has to rotate the island toroidally by varying the absolute phase of the RMP field.

Figure 1 demonstrates the challenge in measuring such an island, where Fig. 1a illustrates rotating magnetic surface perturbations from pure ideal kink modes and Fig. 1b shows a combination of an ideal kink mode and a magnetic island having its o-point (see annotation in Fig. 1b) near the minimum of the kink deformation. This is the o-point

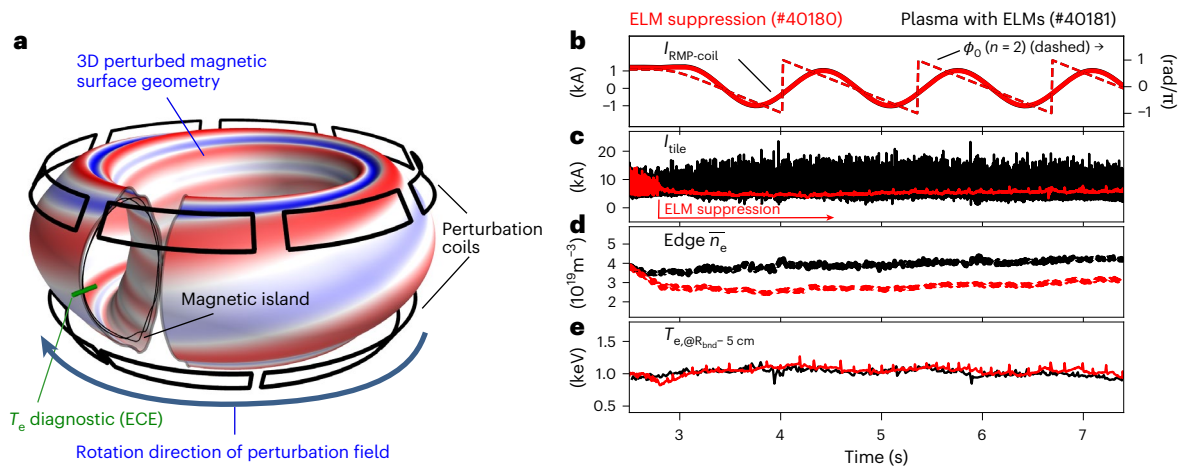


**Fig. 2 | Experimental setup in the ASDEX-Upgrade tokamak.** **a**, The measurement position of the ECE diagnostic to measure plasma surface perturbations via the electron temperature ( $T_e$ ), perturbation (saddle) coils to generate the RMP field and the rotation direction of the perturbation field along the toroidal coordinate. The sketch shows a possible island and the kinking plasma surface, where the deformation outwards is red and inwards blue. **b–e**, Time traces of plasma parameters from the ELM-suppressed (discharge

#40180, red) and ELMy (discharge #40181, black) plasmas during a phase of constant plasma current and heating power: the current of one RMP coil ( $I_{\text{RMP-coil}}$ ) and the varying toroidal phase  $\phi_0$  of the RMP field at the right vertical axis (**b**); current measurements from a wall tile  $I_{\text{tile}}$  to identify ELMs (**c**); the edge-averaged density  $\bar{n}_e$  using line interferometry measurements (**d**); and measured  $T_e$  from ECE roughly 5 cm inside the plasma boundary  $R_{\text{bnd}}$  ( $T_{e,@R_{\text{bnd}}-5\text{cm}}$ ) (**e**).

position expected from vacuum field calculations where the response of the plasma to the RMP field is neglected. The actual o-point position may deviate slightly, but not more than a few tens of degrees, because of drag from a viscous plasma and a local finite electron fluid velocity ( $v_{e,\perp}$ ) in two-fluid MHD<sup>38</sup>. Here,  $v_{e,\perp}$  is the sum of  $\mathbf{E} \times \mathbf{B}$  flow velocity ( $v_{E \times B}$ ) and the electron diamagnetic velocity ( $v_{e,\text{dia}}$ )<sup>38</sup>. Figure 1b emphasizes that a magnetic island might only be detectable by small changes in amplitude and phase compared with the pure ideal MHD response. To identify such a magnetic island, we designed an experiment with rotating RMP fields, which was performed once in ELM-suppressed plasma and once again in an ELMy plasma. In ELM-suppressed experiments, a magnetic island at the pedestal top may cause deviations from ideal MHD, while the subsequent experiment with ELMs serves as a control experiment with no magnetic island at the pedestal top.

The ASDEX-Upgrade tokamak is well suited for this experiment with its flexible RMP coil setup<sup>39</sup> and high-resolution ECE diagnostics<sup>35</sup>. For our experiments, we use the typical plasma discharge configuration to achieve ELM suppression in ASDEX-Upgrade<sup>9</sup> (Methods) with an edge safety factor ( $q_{95}$ ) of 3.7 and an RMP field with  $n = 2$  toroidal field symmetry using 16 ‘saddle’ coils distributed over two rows (Fig. 2). The rational surface  $q = m/n = 7/2$  (where  $m$  denotes the poloidal mode number) is of interest and just inside the pedestal top.

We focus on two consecutive plasma discharges to compare ELM-suppressed (discharge #40180) and ELMy phases (#40181), which differ only by the amount of injected deuterium gas. The RMP field is rotated in the clockwise direction (top-down view) as observed by its continuously decreasing toroidal phase  $\phi_0$  (Fig. 2b), while the alignment of the RMP field remains fixed. The rotation frequency ( $f_{\text{RMP}}$ ) is limited to 0.75 Hz, which is enough to probe three rotation periods during the plasma discharge (Fig. 2b).

ELMs appear as spikes in thermo-electric currents onto a wall tile ( $I_{\text{tile}}$ ; Fig. 2c), which allows to distinguish ELMy-plasma phases from ELM-suppressed ones and to identify timepoints affected by ELMs (Extended Data Fig. 3) The line-averaged electron density ( $\bar{n}_e$ ) at the edge is lower in ELM suppression (Fig. 2d), due to the different gas fuelling and the enhanced particle transport known as density pump-out<sup>6</sup>.  $T_e$  inside the plasma is similar in both discharges (Fig. 2e).

The position control system during these experiments causes periodic movements of the outer plasma boundary position from the

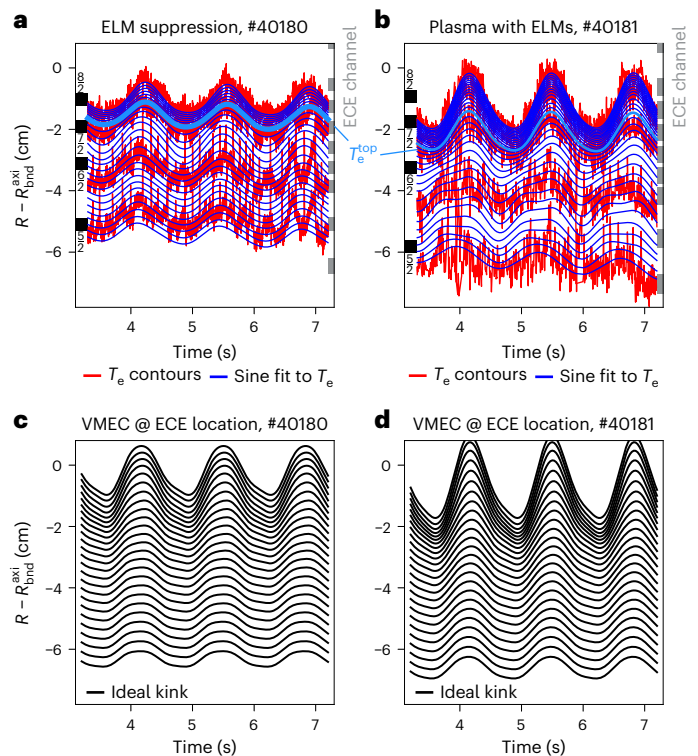


**Fig. 3 | Measured magnetic surface perturbations compared with predicted ideal kink modes.** **a, b**, Measurements of magnetic surface perturbations using electron temperature ( $T_e$ ) contours (red) in 200 eV steps and sinusoidal fits to each contour (blue) in 20 eV steps along the radial coordinate  $R$  of the ECE diagnostic relative to the axisymmetric plasma boundary  $R_{\text{bnd}}^{\text{axi}}$ . This is shown during the RMP field rotation for an ELM-suppressed plasma (discharge #40180) (**a**) and an ELMy plasma (discharge #40181) (**b**) using only data points in-between ELMs. The black bars on the left of **a** and **b** show the averaged position of rational surfaces (6/2, 7/2 and so on). The grey bars indicate averaged ECE channel positions. The thick light-blue lines mark the pedestal top of  $T_e$  ( $T_e^{\text{top}}$ ). **c, d**, The magnetic surface perturbations from predicted ideal kink modes at the ECE measurement position using the VMEC code for ELM-suppressed plasma (**c**) and for ELMy plasma (**d**).

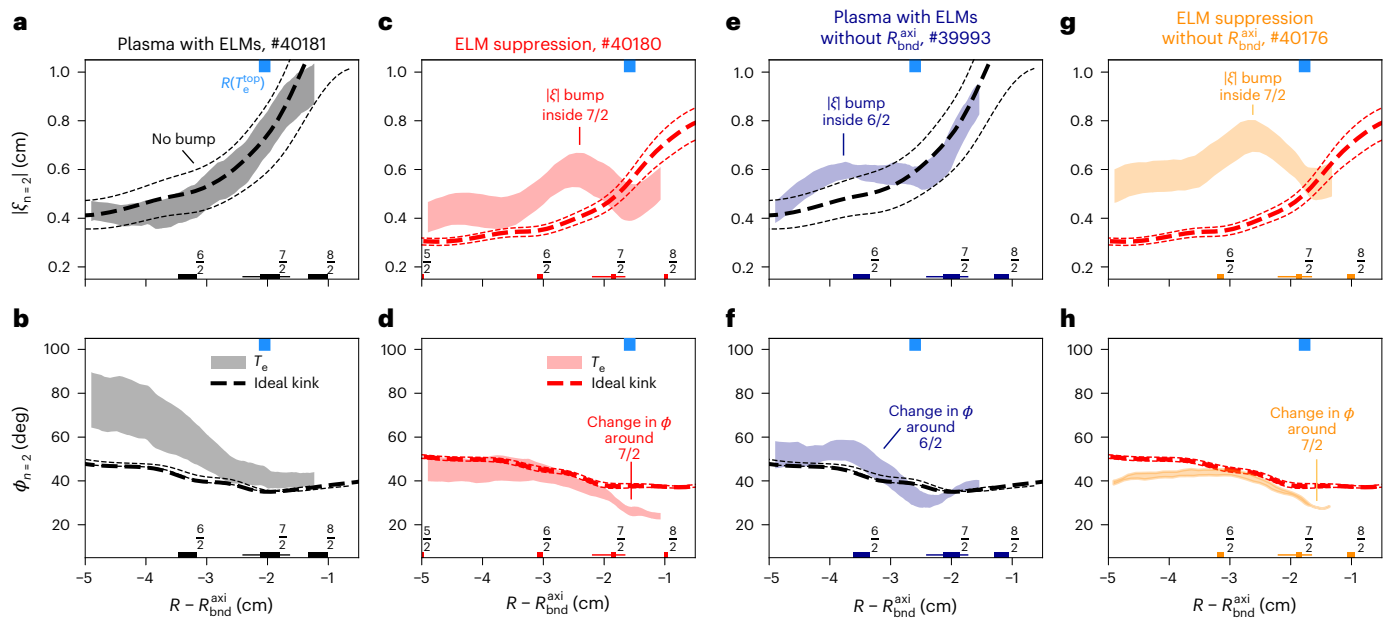


**Fig. 4 | Comparison between measured temperature perturbations and predicted ideal kink modes.** The coloured bands represent the range of measured magnetic surface perturbations derived from electron temperature ( $T_e$ ) measurements, reflecting variations in the analysis (Methods). The dashed line illustrates predictions of ideal kink modes using ideal MHD (VMEC code). The thin lines show deviations from these predictions, indicating uncertainties from the standard deviation in the input pressure profiles. **a, b**, The  $n = 2$  displacement amplitude  $|\xi_{n=2}|$  (**a**) and phase  $\phi_{n=2}$  (**b**) profiles along the radial coordinate of the ECE diagnostic  $R$  relative to the axisymmetric plasma boundary  $R_{bnd}^{axi}$  during phases with ELMs (discharge #40181, black). **c, d**,  $|\xi_{n=2}|$  (**c**) and  $|\phi_{n=2}|$  (**d**) for ELM suppression (#40180, red). **e–h**, Analysis of  $|\xi_{n=2}|$  (**e**) and

$|\phi_{n=2}|$  (**f**) for an ELMy plasma (#39993, blue) as well as  $|\xi_{n=2}|$  (**g**) and  $|\phi_{n=2}|$  (**h**) for an ELM-suppressed plasma (#40176, orange) without the compensation of plasma movements (without  $R_{bnd}^{axi}$ ). Ideal MHD calculations for #40181 (**a** and **b**) and #40180 (**c** and **d**) are reused for #39993 (**e** and **f**) and #40176 (**g** and **h**), respectively. The blue ticks at the top illustrate the mean positions of the pedestal top of the  $T_e$  profiles  $T_e^{top}$ . The boxes at the bottom indicate the rational surfaces ( $6/2$ ,  $7/2$  and so on) and their standard deviation. The horizontal lines at  $7/2$  indicate the uncertainty from various equilibrium calculation methods (Methods). Annotations highlight the differences between measurements and ideal MHD predictions. Data from ref. 50.

axisymmetric equilibrium reconstruction ( $R_{bnd}^{axi}$ ) (see refs. 18,40). These were measured in otherwise identical discharges (#39993 for ELMy and #40176 for ELM suppression) and then compensated. This compensation has minimal impact on the analysis and no impact on our conclusion.

### Comparison of temperature perturbations

To identify a magnetic island, we compare measured  $T_e$  contours to predictions of the ideal kink mode using the 3D ideal MHD code called Variational Moments Equilibrium Code (VMEC)<sup>41</sup> (see Extended Data Fig. 4 for equilibrium properties). VMEC reproduces well the boundary distortion in  $T_e$  and the electron density measured by edge profile diagnostics (Extended Data Fig. 5). Our analysis of  $T_e$  inside the gradient region covers both ELM-suppressed and ELMy plasma phases while the RMP field rotates. Figure 3a,b illustrates measured  $T_e$  contours close to the outer plasma boundary (for the sake of clarity, only four time traces are shown). These contours are analysed relative to  $R_{bnd}^{axi}$  (ordinate in Fig. 3) to take remaining plasma movements into account. To each  $T_e$  contour line, a sine function with higher harmonics is fitted (blue lines shown in 20 eV steps in Fig. 3a,b; see Methods for details). The same fit is applied to magnetic surface perturbations from ideal kink modes as calculated by the VMEC code at the ECE position (Fig. 3c,d).

In the following, we focus on the amplitude and phase of the fundamental ( $n = 2$ ) magnetic surface perturbation around the pedestal top. In ELMy plasmas, the amplitude decreases from the edge towards the core (Fig. 4a, bands), which is in agreement with ideal MHD (Fig. 4a, dashed line). The phase is compared in Fig. 4b and shows no abnormality around the  $7/2$  rational surface where the measured surface

displacement amplitude is sufficiently large to determine the phase accurately. Further inside, in regions of reduced amplitude, differences in phase between the modelling and measurements occur that are outside the uncertainties. As we will discuss later, these are not caused by a magnetic island.

In ELM suppression, the amplitude of the ideal kink is globally reduced due to lower pressure gradients. Moreover, a distinct bump structure in amplitude is observed inside the  $7/2$  surface (Fig. 4c, red) and the phase exhibits a decrease outside of the  $7/2$  surface (Fig. 4d, red). These structures are not observed in the ELMy reference from Fig. 4a,b nor captured by ideal MHD modelling. We would like to emphasize that a bump structure in amplitude without a change in phase may also arise in ideal MHD<sup>36</sup>. However, despite employing varied input pressure profiles and a high-resolution radial grid in our modelling, none of the ideal MHD calculations has yielded a notable bump structure around the  $7/2$  rational surface (Fig. 4, thin lines). As illustrated in Fig. 1, this may indicate the presence of a magnetic island.

Analysis of ELM suppression experiments without the compensation of the outer plasma boundary ( $R_{bnd}^{axi}$ ) movements reveals the same displacement structures around the  $7/2$  surface (Fig. 4g,h, orange) with an additional offset in  $|\xi_{n=2}|$  of about 1 mm. However, the pattern in amplitude and phase around the  $7/2$  surface remains, which consolidates previous observations. In addition, an ELMy experiment from a different session (discharge 39993) with altered wall conditions due to preceding high-fuelling experiments shows similar structures around the  $6/2$  surface (Fig. 4e,f, blue), suggesting the presence of an island at this surface. However, this  $6/2$  island did not lead to ELM suppression in this discharge.

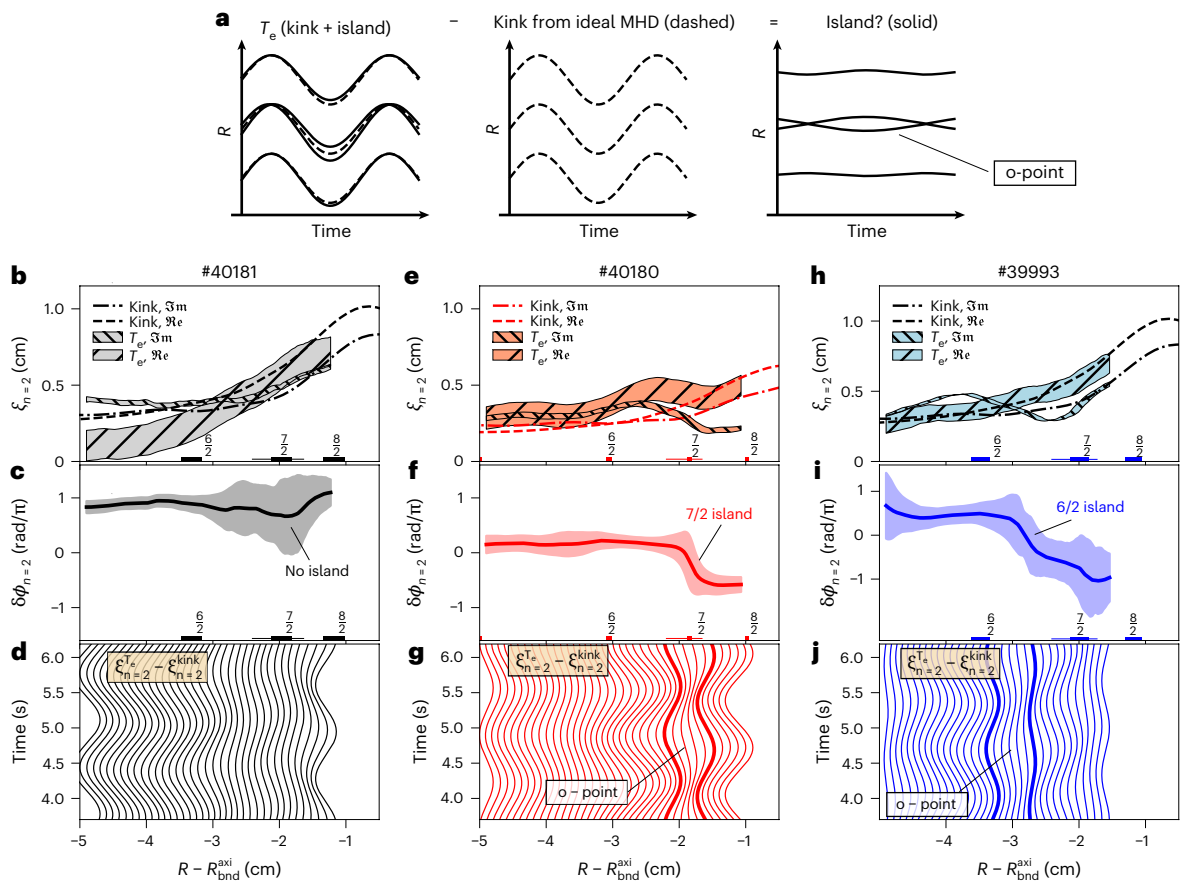


**Fig. 5 | Analysis to identify magnetic island structure.** **a**, The method of subtracting the kink component based on ideal MHD calculations from electron temperature  $T_e$  measurements along a radial coordinate  $R$  to uncover a potential island structure. **b, e, h**, Real  $\Re e$  and imaginary  $\Im m$   $n = 2$  components of the displacement  $\xi_{n=2}$  from the ideal kink mode (dashed and dashed-dotted lines; uncertainties not shown for the sake of clarity) and  $T_e$  measurements (the coloured bands represent the range resulting from variations in the analysis; Methods) versus  $R$  relative to the axisymmetric plasma boundary  $R_{\text{bnd}}^{\text{axi}}$  for the case with ELMy (**b**), ELM suppression (**e**) and the second ELMy case (**h**). The boxes illustrate rational surface positions ( $6/2$ ,  $7/2$  and so on), and the horizontal lines

at the  $7/2$  box indicate the uncertainty from various equilibrium calculation methods (Methods). **c, f, i**, The analysed phase  $\delta\phi_{n=2}$  from equation (1) for the ELMy case (**c**), ELM suppression (**f**) and the second ELMy case (**i**). **d, g, j**, The difference between measured displacement  $\xi_{n=2}^{T_e}$  and ideal kink components  $\xi_{n=2}^{\text{kink}}$ , revealing the island structure, which is emphasized by thick lines, and the o-point is annotated for the ELM suppression case (**g**) and the second ELMy case (**j**). No island structure is seen in the ELMy case (**d**). The ELM suppression case shows a clear jump in phase and island structure around the  $7/2$  rational surface, whereas ELMy plasmas show either a phase jump at a position further inside ( $6/2$  island) or no phase jump at all.

### Identifying magnetic islands

To analyse the origin of the observed features in the displacement, we assume that  $T_e$  measurements comprise an ideal kink mode and a potential magnetic island (see Fig. 5a for illustration). To disentangle both, we first define the imaginary components of the  $n = 2$  displacement using  $\xi_{n=2}^{\Im m} = |\xi_{n=2}| \sin(\phi_{n=2})$  and  $\xi_{n=2}^{\Re e} = |\xi_{n=2}| \cos(\phi_{n=2})$  for real components. The resulting complex components from the modelled ideal kink modes and the measured  $T_e$  contours are shown in Fig. 5b, e, h. In the ELMy case, they agree well around the  $7/2$  rational surface and show the same trend but with small deviations further inside, explaining the differences in the phase observed in Fig. 4b. Unlike the ELMy reference, the ELM suppression case exhibits pronounced differences in the complex components around the  $7/2$  surface (Fig. 5e). To isolate a possible magnetic island structure, we subtract the ideal kink components from the measured ones and calculate the resulting phase via

$$\delta\phi_{n=2} = \arctan \left( \frac{\xi_{n=2}^{\Im m, T_e} - \xi_{n=2}^{\Im m, \text{kink}}}{\xi_{n=2}^{\Re e, T_e} - \xi_{n=2}^{\Re e, \text{kink}}} \right). \quad (1)$$

A potential magnetic island is then detected via a jump in phase  $\delta\phi_{n=2}$  by about  $\pi$  (ref. 36). The analysed phase shows no jump for the

ELMy case (Fig. 5c), whereas a clear phase jump by  $\pi$  close to the  $7/2$  surface is seen during ELM suppression (Fig. 5f). In addition, we apply the same procedure to the ELMy case with a similar structure around the  $6/2$  surface (Fig. 5f) (note, here the VMEC calculations from Fig. 5b have been reused). A phase jump by around  $\pi$  is also observed around the  $6/2$  surface, suggesting the presence of a  $6/2$  magnetic island. Figure 5d, g, j illustrates the underlying magnetic island structures by subtracting the magnetic surface perturbations of the ideal kink modes from the measured ones. A magnetic island is observed at the pedestal top in the ELM suppression case, whereas one ELMy case shows no structure and the other one a magnetic island close to the  $6/2$  rational surface. This single  $6/2$  island, which is located deeper inside the plasma and not at the pedestal top, is apparently not in conjunction with ELM suppression.

Note that the presented analysis of  $\delta\phi_{n=2}$  should be approached with caution, since it depends strongly on the agreement between  $T_e$  and ideal MHD modelling or, rather, on the distortions being dominated by ideal MHD. This dependency is evident in the increased uncertainties observed in the ELMy case (Fig. 5c), attributed to larger uncertainties coming from the experimental data used for the modelling input. Thus, the strongest evidence for the presence of a magnetic island lies in the observed structures in the displacement amplitude (Fig. 4c, e, g) and the

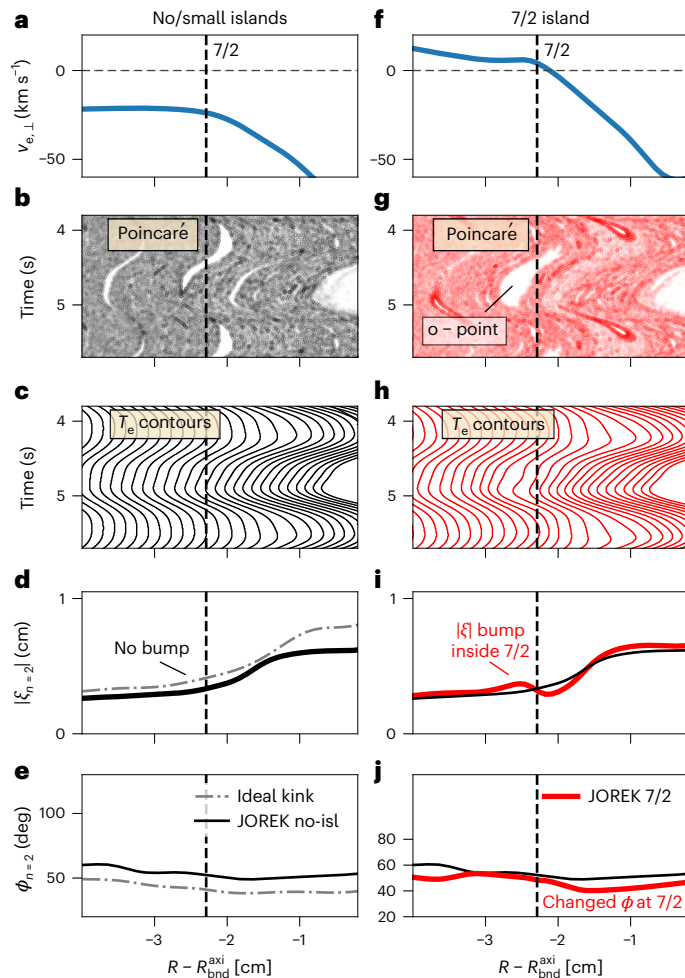


**Fig. 6 | Magnetic island in nonlinear resistive MHD calculations from JOREK.**

Comparison between two different calculations based on data from the ELM suppression case employing different torque sources. The left column shows the following parameters at the radial coordinate  $R$  relative to the axisymmetric plasma boundary  $R_{\text{bnd}}^{\text{axi}}$  from JOREK: the fluid velocity of the electrons  $v_{e,\perp}$  averaged over the toroidal coordinate (a), a scatter plot of magnetic field lines crossing the toroidal plane at the ECE location (Poincaré plot) (b), electron temperature  $T_e$  contour lines (c),  $n = 2$  displacement amplitude  $|\xi_{n=2}|$  (d) and  $n = 2$  phase  $\phi_{n=2}$  from simulated  $T_e$  without large islands ('no-isl',  $<1.5$  mm) showing 'no bump' in amplitude and agreeing with ideal MHD predictions (dashed-dotted) (e). The right column shows  $v_{e,\perp}$  (f), Poincaré plot (g),  $T_e$  contours (h),  $|\xi_{n=2}|$  (i) and  $|\phi_{n=2}|$  (j) from calculations with a 7/2 island of 4 mm size. The o-point is annotated in g, i and j compare simulations with 7/2 island (red) and without (black), and differences are annotated.

complex component profiles (Fig. 5b,e,h) around the rational surfaces, which are not captured by ideal MHD modelling.

### Nonlinear resistive MHD calculations

To get further confidence that the observed structures in  $T_e$  originate from magnetic islands, we utilized the resistive MHD code called JOREK<sup>42</sup>. JOREK modelling of ASDEX-Upgrade experiments with RMPs<sup>43</sup> has made advances allowing the calculation of the plasma response to the RMP field with realistic viscosity, with free boundary<sup>44</sup> and realistic anisotropy between parallel and perpendicular electron heat transport.

We aim for a qualitative comparison and conducted a numerical experiment based on the presented ELM suppression case (discharge #40180). To underline that the observed structures, that is, the bump in amplitude of the displacement, originate from an island, we varied

the torque source to perform a scan over different  $v_{e,\perp}$  profiles. As mentioned previously,  $v_{e,\perp}$  is decisive for the formation of magnetic islands in two-fluid MHD<sup>38</sup>. One simulation has strongly negative  $v_{e,\perp}$  and, therefore, develops no or only very small magnetic islands (Fig. 6a–e). This simulation is also in good agreement with predictions from ideal MHD (Fig. 6d,e). The second simulation has a zero-crossing of  $v_{e,\perp}$  at the 7/2 rational surface, which allows the formation of a single magnetic island at the pedestal top (Fig. 6f–j).

The simulated  $T_e$  contours illustrate that the induced magnetic island causes the same features as observed in the experiment such as the bump in amplitude. This structure is not visible in the simulation without islands. The simulated magnetic island has a size of roughly 4 mm, which is seen in Fig. 6g and in the distance between the local minima and maxima of the perturbation amplitude (Fig. 6i). The latter is often used as a proxy for the island size<sup>36</sup> and amounts to  $W_{\text{ECE}} = 9$  mm in the  $T_e$  measurements. There is also a small change in phase, but one should note that this is strongly influenced by the island size and its position, which depends on the local  $v_{e,\perp}$  (ref. 38). It may even vanish when the island's o-point position aligns with one of the vacuum island's positions, coinciding with the minimum displacement of the ideal kink mode. Although the JOREK simulations show a smaller island size attributed to constraints within its MHD description (Methods), all key features of the measurements are reproduced.

### Discussion and island size

We are aware that our numerical experiment with JOREK using the zero-crossing of  $v_{e,\perp}$  is in contrast to experimental observations showing no zero-crossing<sup>9,45</sup>. However, plasma response modelling including kinetic effects highlights the importance of  $v_{E \times B} = 0$  for the penetration of magnetic islands<sup>46</sup>. In addition, recent experiments showed strongly non-axisymmetric radial electric field ( $E_r$ ) profiles at the edge in the presence of RMPs<sup>31</sup>. To determine accurately  $v_{e,\perp}$  (ref. 25) and  $v_{E \times B}$  (ref. 46) at the plasma edge requires elaborate analysis taking 3D effects into account, which is beyond the scope of this article.

We estimate an island size of  $W_{\text{ECE}} \approx 1$  cm at the ECE position, which corresponds to an island size averaged over the magnetic surface  $\overline{W}_{\text{isl}}$  of 2 cm. This is roughly 1% of the major radius and is in the same order of magnitude as modelling results of a magnetic island during ELM suppression in a tokamak with similar size<sup>26</sup>. The measured island size is twice the critical island width  $\overline{W}_{\text{crit}}$  of 1 cm from ref. 34. At this size, a complete flat  $T_e$  profile at the o-point is not expected and is also not observed by the ECE diagnostic. Further numerical studies are required to determine if the estimated island size is sufficient to explain the drop in temperature and density, or if additional mechanisms inter-playing with the magnetic island such as turbulence<sup>31,47</sup>, electron polarization drift<sup>26</sup>, neoclassical transport<sup>48</sup> and nonlinear mode coupling<sup>43,48,49</sup> are involved.

### Online content

Any methods, additional references, Nature Portfolio reporting summaries, source data, extended data, supplementary information, acknowledgements, peer review information; details of author contributions and competing interests; and statements of data and code availability are available at <https://doi.org/10.1038/s41567-024-02666-y>.

### References

1. Wade, M. R. & Leuer, J. A. Cost drivers for a tokamak-based compact pilot plant. *Fusion Sci. Technol.* **77**, 119–143 (2021).
2. Wagner, F. et al. Regime of improved confinement and high beta in neutral-beam-heated divertor discharges of the ASDEX tokamak. *Phys. Rev. Lett.* **49**, 1408–1412 (1982).
3. Ham, C., Kirk, A., Pamela, S. & Wilson, H. Filamentary plasma eruptions and their control on the route to fusion energy. *Nat. Rev. Phys.* **2**, 159–167 (2020).

4. Eich, T. et al. ELM divertor peak energy fluence scaling to ITER with data from JET, MAST and ASDEX Upgrade. *Nucl. Mater. Energy* **12**, 84–90 (2017).
5. Wenninger, R. P. et al. DEMO divertor limitations during and in between ELMs. *Nucl. Fusion* **54**, 114003 (2014).
6. Evans, T. E. et al. Edge stability and transport control with resonant magnetic perturbations in collisionless tokamak plasmas. *Nat. Phys.* **2**, 419–423 (2006).
7. Sun, Y. et al. Nonlinear transition from mitigation to suppression of the edge localized mode with resonant magnetic perturbations in the EAST tokamak. *Phys. Rev. Lett.* **117**, 115001 (2016).
8. Park, J.-k et al. 3D field phase-space control in tokamak plasma. *Nat. Phys.* **14**, 1223–1228 (2018).
9. Suttrop, W. et al. Experimental conditions to suppress edge localised modes by magnetic perturbations in the ASDEX Upgrade tokamak. *Nucl. Fusion* **58**, 096031 (2018).
10. Shousha, R. et al. Design and experimental demonstration of feedback adaptive RMP ELM controller toward complete long pulse ELM suppression on KSTAR. *Phys. Plasmas* **29**, 032514 (2022).
11. Huijsmans, G. T. A. et al. Modelling of edge localised modes and edge localised mode control. *Phys. Plasma* **22**, 021805 (2015).
12. Sweeney, R. et al. MHD stability and disruptions in the SPARC tokamak. *J. Plasma Phys.* **86**, 865860507 (2020).
13. Ongena, J., Koch, R., Wolf, R. & Zohm, H. Magnetic-confinement fusion. *Nat. Phys.* **12**, 398–410 (2016).
14. Nardon, E., Tamain, P., Bécoulet, M., Huysmans, G. & Waelbroeck, F. L. Quasi-linear MHD modelling of H-mode plasma response to resonant magnetic perturbations. *Nucl. Fusion* **50**, 034002 (2010).
15. Park, J.-k, Boozer, A. H. & Glasser, A. H. Computation of three-dimensional tokamak and spherical torus equilibria. *Phys. Plasma* **14**, 052110 (2007).
16. Lanctot, M. J. et al. Measurement and modeling of three-dimensional equilibria in DIII-D. *Phys. Plasma* **18**, 056121 (2011).
17. Chapman, I. T. et al. Three-dimensional distortions of the tokamak plasma boundary: boundary displacements in the presence of resonant magnetic perturbations. *Nucl. Fusion* **54**, 083006 (2014).
18. Willensdorfer, M. et al. Three dimensional boundary displacement due to stable ideal kink modes excited by external  $n = 2$  magnetic perturbations. *Nucl. Fusion* **57**, 116047 (2017).
19. Willensdorfer, M. et al. Dynamics of ideal modes and subsequent ELM crashes in 3D tokamak geometry from external magnetic perturbations. *Plasma Phys. Control. Fusion* **61**, 014019 (2019).
20. Snyder, P. B. et al. The EPED pedestal model and edge localized mode-suppressed regimes: studies of quiescent H-mode and development of a model for edge localized mode suppression via resonant magnetic perturbations. *Phys. Plasma* **19**, 056115 (2012).
21. Paz-Soldan, C. et al. Observation of a multimode plasma response and its relationship to density pumpout and edge-localized mode suppression. *Phys. Rev. Lett.* **114**, 105001 (2015).
22. Ryan, D. A. et al. Toroidal modelling of resonant magnetic perturbations response in ASDEX-Upgrade: coupling between field pitch aligned response and kink amplification. *Plasma Phys. Control. Fusion* **57**, 095008 (2015).
23. Nazikian, R. et al. Pedestal bifurcation and resonant field penetration at the threshold of edge-localized mode suppression in the DIII-D tokamak. *Phys. Rev. Lett.* **114**, 105002 (2015).
24. Wade, M. R. et al. Advances in the physics understanding of ELM suppression using resonant magnetic perturbations in DIII-D. *Nucl. Fusion* **55**, 023002 (2015).
25. Moyer, R. A. et al. Validation of the model for ELM suppression with 3D magnetic fields using low torque ITER baseline scenario discharges in DIII-D. *Phys. Plasma* **24**, 102501 (2017).
26. Hu, Q. M. et al. The role of edge resonant magnetic perturbations in edge-localized-mode suppression and density pump-out in low-collisionality DIII-D plasmas. *Nucl. Fusion* **60**, 076001 (2020).
27. Hu, Q. M. et al. Predicting operational windows of ELMs suppression by resonant magnetic perturbations in the DIII-D and KSTAR tokamaks. *Phys. Plasmas* **28**, 052505 (2021).
28. Fitzpatrick, R. Modeling  $q_{95}$  windows for the suppression of edge localized modes by resonant magnetic perturbations in the DIII-D tokamak. *Phys. Plasma* **27**, 102511 (2020).
29. Gu, S. et al. Edge localized mode suppression and plasma response using mixed toroidal harmonic resonant magnetic perturbations in DIII-D. *Nucl. Fusion* **59**, 026012 (2019).
30. King, J. D. et al. Three-dimensional equilibria and island energy transport due to resonant magnetic perturbation edge localized mode suppression on DIII-D. *Phys. Plasma* **22**, 112502 (2015).
31. Leuthold, N. et al. Turbulence characterization during the suppression of edge-localized modes by magnetic perturbations on ASDEX Upgrade. *Nucl. Fusion* **63**, 046014 (2023).
32. Nazikian, R. et al. Advances in the understanding of ELM suppression by resonant magnetic perturbations (RMPs) in DIII-D and implications for ITER. In *IAEA Conference Proceeding* (IAEA, 2014); <https://www.osti.gov/servlets/purl/1182663>
33. Willensdorfer, M. et al. Plasma response measurements of external magnetic perturbations using electron cyclotron emission and comparisons to 3D ideal MHD equilibrium. *Plasma Phys. Control. Fusion* **58**, 114004 (2016).
34. Fitzpatrick, R. Helical temperature perturbations associated with tearing modes in tokamak plasmas. *Phys. Plasma* **2**, 825–838 (1995).
35. Denk, S. S. et al. Analysis of electron cyclotron emission with extended electron cyclotron forward modeling. *Plasma Phys. Control. Fusion* **60**, 105010 (2018).
36. Gude, A. in *Active Control of Magneto-hydrodynamic Instabilities in Hot Plasmas* Vol. 83 (ed. Igochine, V.) 53–104 (Springer, 2015); [https://doi.org/10.1007/978-3-662-44222-7\\_3](https://doi.org/10.1007/978-3-662-44222-7_3)
37. Igochine, V. et al. Tearing mode formation induced by internal crash events at different  $\beta_N$ . *Nucl. Fusion* **57**, 036015 (2017).
38. Yu, Q., Günter, S., Kikuchi, Y. & Finken, K. H. Numerical modelling of error field penetration. *Nucl. Fusion* **48**, 024007 (2008).
39. Suttrop, W. et al. Studies of edge localized mode mitigation with new active in-vessel saddle coils in ASDEX Upgrade. *Plasma Phys. Control. Fusion* **53**, 124014 (2011).
40. Chapman, I. T. et al. The effect of the plasma position control system on the three-dimensional distortion of the plasma boundary when magnetic perturbations are applied in MAST. *Plasma Phys. Control. Fusion* **56**, 075004 (2014).
41. Hirshman, S. P., van Rij, W. I. & Merkel, P. Three-dimensional free boundary calculations using a spectral Green's function method. *Comput. Phys. Commun.* **43**, 143–155 (1986).
42. Hoelzl, M. et al. The JOREK non-linear extended MHD code and applications to large-scale instabilities and their control in magnetically confined fusion plasmas. *Nucl. Fusion* **61**, 065001 (2021).
43. Orain, F. et al. Non-linear modeling of the plasma response to RMPs in ASDEX Upgrade. *Nucl. Fusion* **57**, 022013 (2017).
44. Mitterauer, V. et al. Non-linear free boundary simulations of the plasma response to resonant magnetic perturbations in ASDEX Upgrade plasmas. *J. Phys. Conf. Series* **2397**, 012008 (2022).
45. Paz-Soldan, C. et al. The effect of plasma shape and neutral beam mix on the rotation threshold for RMP-ELM suppression. *Nucl. Fusion* **59**, 056012 (2019).
46. Heyn, M. F. et al. Quasilinear modelling of RMP interaction with a tokamak plasma: application to ASDEX Upgrade ELM mitigation experiments. *Nucl. Fusion* **54**, 064005 (2014).

47. Hager, R., Chang, C. S., Ferraro, N. M. & Nazikian, R. Gyrokinetic understanding of the edge pedestal transport driven by resonant magnetic perturbations in a realistic divertor geometry. *Phys. Plasmas* **27**, 062301 (2020).
48. Kim, S. K. et al. Nonlinear MHD modeling of  $n = 1$  RMP-induced pedestal transport and mode coupling effects on ELM suppression in KSTAR. *Nucl. Fusion* **62**, 106021 (2022).
49. B'ecoulet, M. et al. Mechanism of edge localized mode mitigation by resonant magnetic perturbations. *Phys. Rev. Lett.* **113**, 115001 (2014).
50. Zohm, H. et al. Overview of ASDEX Upgrade results in view of ITER and DEMO. *Nucl. Fusion* **64**, 112001 (2024).

**Open Access** This article is licensed under a Creative Commons Attribution 4.0 International License, which permits use, sharing, adaptation, distribution and reproduction in any medium or format, as long as you give appropriate credit to the original author(s) and the source, provide a link to the Creative Commons licence, and indicate if changes were made. The images or other third party material in this article are included in the article's Creative Commons licence, unless indicated otherwise in a credit line to the material. If material is not included in the article's Creative Commons licence and your intended use is not permitted by statutory regulation or exceeds the permitted use, you will need to obtain permission directly from the copyright holder. To view a copy of this licence, visit <http://creativecommons.org/licenses/by/4.0/>.

**Publisher's note** Springer Nature remains neutral with regard to jurisdictional claims in published maps and institutional affiliations.

© The Author(s) 2024

## the ASDEX Upgrade Team

D. Aguiam<sup>6</sup>, E. Alessi<sup>7</sup>, C. Angioni<sup>1</sup>, N. Arden<sup>1</sup>, V. Artigues<sup>1</sup>, M. Astrain<sup>1</sup>, O. Asunta<sup>8</sup>, M. Balden<sup>1</sup>, V. Bandaru<sup>1</sup>, A. Banon Navarro<sup>1</sup>, M. Bauer<sup>1</sup>, A. Bergmann<sup>1</sup>, M. Bergmann<sup>1</sup>, J. Bernardo<sup>6</sup>, M. Bernert<sup>1</sup>, A. Biancalani<sup>9</sup>, R. Bielajew<sup>10</sup>, R. Bilato<sup>1</sup>, G. Birkenmeier<sup>1</sup>, T. Blanken<sup>11</sup>, V. Bobkov<sup>1</sup>, A. Bock<sup>1</sup>, L. Bock<sup>1</sup>, T. Body<sup>1</sup>, T. Bolzonella<sup>12</sup>, N. Bonanomi<sup>1</sup>, A. Bortolon<sup>13</sup>, B. Bösowirh<sup>1</sup>, C. Bottereau<sup>14</sup>, A. Bottino<sup>1</sup>, H. van den Brand<sup>11</sup>, M. Brenzke<sup>15</sup>, S. Brezinsek<sup>15</sup>, D. Brida<sup>1</sup>, F. Brochard<sup>16</sup>, J. Buchanan<sup>17</sup>, A. Buhler<sup>1</sup>, A. Burckhart<sup>1</sup>, Y. Camenen<sup>18</sup>, B. Cannas<sup>19</sup>, P. Cano Megias<sup>1</sup>, D. Carlton<sup>1</sup>, M. Carr<sup>17</sup>, P. Carvalho<sup>6</sup>, C. Castaldo<sup>20</sup>, A. Castillo Castillo<sup>1</sup>, M. Cavedon<sup>21</sup>, C. Cazzaniga<sup>12</sup>, C. Challis<sup>17</sup>, A. Chankin<sup>1</sup>, A. Chomiczewska<sup>22</sup>, C. Cianfarani<sup>20</sup>, F. Clairet<sup>14</sup>, S. Coda<sup>23</sup>, R. Coelho<sup>6</sup>, J. W. Coenen<sup>15</sup>, L. Colas<sup>14</sup>, G. Conway<sup>1</sup>, S. Costea<sup>24</sup>, D. Coster<sup>1</sup>, T. Cote<sup>25</sup>, A. J. Creely<sup>26</sup>, G. Croci<sup>7</sup>, D. J. Cruz Zabala<sup>27</sup>, G. Cseh<sup>28</sup>, I. Cziegler<sup>29</sup>, O. D'Arcangelo<sup>30</sup>, A. Dal Molin<sup>21</sup>, P. David<sup>1</sup>, C. Day<sup>31</sup>, M. de Baar<sup>11</sup>, P. de Marné<sup>1</sup>, R. Delogu<sup>12</sup>, P. Denner<sup>15</sup>, A. Di Siena<sup>1</sup>, M. Dibon<sup>1</sup>, J. J. Dominguez Palacios Durán<sup>27</sup>, D. Dunai<sup>28</sup>, M. Dreval<sup>32</sup>, M. Dunne<sup>1</sup>, B. P. Duval<sup>23</sup>, R. Dux<sup>1</sup>, T. Eich<sup>26</sup>, S. Elgeti<sup>1</sup>, A. Encheva<sup>4</sup>, B. Esposito<sup>20</sup>, E. Fable<sup>1</sup>, M. Faitsch<sup>1</sup>, D. Fajardo Jimenez<sup>1</sup>, U. Fantz<sup>1</sup>, M. Farnik<sup>33</sup>, H. Faugel<sup>1</sup>, F. Felici<sup>23</sup>, O. Ficker<sup>33</sup>, A. Figueredo<sup>6</sup>, R. Fischer<sup>1</sup>, O. Ford<sup>34</sup>, L. Frassinetti<sup>35</sup>, M. Fröschle<sup>1</sup>, G. Fuchert<sup>34</sup>, J. C. Fuchs<sup>1</sup>, H. Fünfgelder<sup>1</sup>, S. Futatani<sup>36</sup>, K. Galazka<sup>22</sup>, J. Galdon-Quiroga<sup>27</sup>, D. Gallart Escolà<sup>36</sup>, A. Gallo<sup>14</sup>, Y. Gao<sup>15</sup>, S. Garavaglia<sup>7</sup>, M. Garcia Muñoz<sup>27</sup>, B. Geiger<sup>25</sup>, L. Giannone<sup>1</sup>, S. Gibson<sup>37</sup>, L. Gil<sup>6</sup>, E. Giovannozzi<sup>20</sup>, O. Girka<sup>1</sup>, T. Gleiter<sup>1</sup>, S. Glöggler<sup>15</sup>, M. Gobbin<sup>12</sup>, J. C. Gonzalez<sup>1</sup>, J. Gonzalez Martin<sup>27</sup>, T. Goodman<sup>23</sup>, G. Gorini<sup>21</sup>, T. Görler<sup>1</sup>, D. Gradic<sup>34</sup>, G. Granucci<sup>7</sup>, A. Gräter<sup>1</sup>, G. Grenfell<sup>1</sup>, H. Greuner<sup>1</sup>, M. Griener<sup>1</sup>, M. Groth<sup>8</sup>, O. Grover<sup>1</sup>, A. Gude<sup>1</sup>, L. Guimarais<sup>6</sup>, S. Günter<sup>1</sup>, D. Hachmeister<sup>6</sup>, A. H. Hakola<sup>38</sup>, C. Ham<sup>17</sup>, T. Happel<sup>1</sup>, N. den Harder<sup>1</sup>, G. Harre<sup>39</sup>, J. Harrison<sup>17</sup>, V. Hauer<sup>31</sup>, T. Huymard-Schneider<sup>1</sup>, B. Heinemann<sup>1</sup>, P. Heinrich<sup>1</sup>, T. Hellsten<sup>40</sup>, S. Henderson<sup>17</sup>, P. Hennequin<sup>41</sup>, S. Heuraux<sup>16</sup>, A. Herrmann<sup>1</sup>, E. Heyn<sup>42</sup>, F. Hitzler<sup>5</sup>, J. Hobirk<sup>1</sup>, K. Höfler<sup>34</sup>, J. H. Holm<sup>43</sup>, M. Hölzl<sup>1</sup>, C. Hopf<sup>1</sup>, L. Horvath<sup>29</sup>, T. Höschen<sup>1</sup>, A. Houben<sup>16</sup>, A. Hubbard<sup>10</sup>, A. Huber<sup>15</sup>, K. Hunger<sup>1</sup>, V. Igochine<sup>1</sup>, M. Iliasova<sup>44</sup>, J. Illerhaus<sup>1</sup>, K. Insulander Björk<sup>45</sup>, C. Ionita-Schrittwieser<sup>24</sup>, I. Ivanova-Stanik<sup>22</sup>, S. Jachmich<sup>4</sup>, W. Jacob<sup>1</sup>, N. Jaksic<sup>1</sup>, F. Janky<sup>1</sup>, A. Jansen van Vuuren<sup>27</sup>, F. Jaulmes<sup>33</sup>, F. Jenko<sup>1</sup>, T. Jensen<sup>43</sup>, E. Joffrin<sup>14</sup>, A. Kallenbach<sup>1</sup>, J. Kalis<sup>1</sup>, M. Kantor<sup>11</sup>, A. Kappatou<sup>1</sup>, J. Karhunen<sup>8</sup>, C.-P. Käsemann<sup>1</sup>, S. Kasilov<sup>42</sup>, Y. Kazakov<sup>46</sup>, A. Kendl<sup>24</sup>, W. Kernbichler<sup>39</sup>, E. Khilkvitch<sup>44</sup>, M. Kircher<sup>1</sup>, A. Kirk<sup>17</sup>, S. Kjer Hansen<sup>43</sup>, V. Klevarova<sup>47</sup>, F. Klossek<sup>1</sup>, G. Kocsis<sup>28</sup>, M. Koleva<sup>1</sup>, M. Komm<sup>33</sup>, M. Kong<sup>23</sup>, A. Krämer-Flecken<sup>15</sup>, M. Krause<sup>1</sup>, A. Kreuzeder<sup>1</sup>, K. Krieger<sup>1</sup>, O. Kudlacek<sup>1</sup>, D. Kulla<sup>34</sup>, T. Kurki-Suonio<sup>8</sup>, B. Kurzan<sup>1</sup>, B. Labit<sup>23</sup>, K. Lackner<sup>1</sup>, F. Laggner<sup>13</sup>, A. Lahtinen<sup>8</sup>, P. Lainer<sup>39</sup>, P. T. Lang<sup>1</sup>, P. Lauber<sup>1</sup>, M. Lehnen<sup>4</sup>, E. Lerche<sup>1</sup>, N. Leuthold<sup>3</sup>, L. Li<sup>15</sup>, J. Likonen<sup>38</sup>, O. Linder<sup>1</sup>, B. Lipschultz<sup>29</sup>, Y. Liu<sup>40</sup>, Z. Lu<sup>1</sup>, T. Luda di Cortemiglia<sup>1</sup>, N. C. Luhmann<sup>48</sup>, T. Lunt<sup>1</sup>, A. Lysoivan<sup>46</sup>, T. Maceina<sup>1</sup>, J. Madsen<sup>43</sup>, A. Magnanimo<sup>1</sup>, H. Maier<sup>1</sup>, J. Mailloux<sup>17</sup>, R. Maingi<sup>13</sup>, O. Maj<sup>1</sup>, E. Maljaars<sup>11</sup>, V. Maquet<sup>46</sup>, A. Mancini<sup>7</sup>, A. Manhard<sup>1</sup>, P. Mantica<sup>7</sup>, M. Mantsinen<sup>36,49</sup>, P. Manz<sup>50</sup>, M. Maraschek<sup>1</sup>, C. Marchetto<sup>51</sup>, M. Markl<sup>39</sup>, L. Marrelli<sup>12</sup>, P. Martin<sup>12</sup>, F. Matos<sup>1</sup>, M. Mayer<sup>1</sup>, M.-L. Mayoral<sup>17</sup>, P. J. McCarthy<sup>52</sup>, R. McDermott<sup>1</sup>, R. Merkel<sup>1</sup>, A. Merle<sup>23</sup>, H. Meyer<sup>17</sup>, M. Michelini<sup>1</sup>, D. Milanese<sup>51</sup>, P. Molina Cabrera<sup>1</sup>, M. Muraca<sup>1</sup>, F. Nabais<sup>6</sup>, V. Naulin<sup>43</sup>, R. Nazikian<sup>13</sup>, R. D. Nem<sup>43</sup>, R. Neu<sup>1,53</sup>, A. H. Nielsen<sup>43</sup>, S. K. Nielsen<sup>43</sup>, T. Nishizawa<sup>1</sup>, M. Nocente<sup>21</sup>, I. Novikau<sup>1</sup>, S. Nowak<sup>7</sup>, R. Oouchkov<sup>1</sup>, J. Olsen<sup>43</sup>, P. Oyola<sup>27</sup>, O. Pan<sup>1</sup>, G. Papp<sup>1</sup>, I. Paradela Perez<sup>8</sup>, A. Pau<sup>23</sup>, G. Pautasso<sup>1</sup>, C. Paz-Soldan<sup>3</sup>, M. Peglau<sup>1</sup>, E. Peluso<sup>54</sup>, P. Petersson<sup>35</sup>, C. Piron<sup>12</sup>, U. Plank<sup>1</sup>, B. Plaum<sup>55</sup>, B. Plöckl<sup>1</sup>, V. Plyusnin<sup>6</sup>, G. Pokol<sup>28,56</sup>, E. Poli<sup>1</sup>, L. Porte<sup>23</sup>, J. Puchmayr<sup>1</sup>, T. Pütterich<sup>1</sup>, L. Radovanovic<sup>39</sup>, M. Ramisch<sup>55</sup>, J. Rasmussen<sup>43</sup>, G. Ratta<sup>57</sup>, S. Ratynskaia<sup>35</sup>, G. Raupp<sup>1</sup>, A. Redl<sup>58</sup>, D. Réfy<sup>28</sup>, M. Reich<sup>1</sup>, F. Reimold<sup>34</sup>, D. Reiser<sup>15</sup>, M. Reisner<sup>1</sup>, D. Reiter<sup>15</sup>, B. Rettino<sup>1</sup>, T. Ribeiro<sup>1</sup>, D. Ricci<sup>7</sup>, R. Riedl<sup>1</sup>, J. Riesch<sup>1</sup>, J. F. Rivero Rodriguez<sup>27</sup>, G. Rocchi<sup>20</sup>, P. Rodriguez-Fernandez<sup>10</sup>, V. Rohde<sup>1</sup>, G. Ronchi<sup>11</sup>, M. Rott<sup>1</sup>, M. Rubel<sup>35</sup>, D. A. Ryan<sup>17</sup>, F. Ryter<sup>1</sup>, S. Saarelma<sup>17</sup>, M. Salewski<sup>43</sup>, A. Salmi<sup>8</sup>, O. Samoylov<sup>1</sup>, L. Sanchis Sanchez<sup>27</sup>, J. Santos<sup>6</sup>, O. Sauter<sup>23</sup>, G. Schall<sup>1</sup>, A. Schlüter<sup>1</sup>, J. Scholte<sup>11</sup>, K. Schmid<sup>1</sup>, O. Schmitz<sup>25</sup>, P. A. Schneider<sup>1</sup>, R. Schrittwieser<sup>24</sup>, M. Schubert<sup>1</sup>, C. Schuster<sup>1</sup>, T. Schwarz-Selinger<sup>1</sup>, J. Schweinzer<sup>1</sup>, F. Sciortino<sup>1</sup>, O. Seibold-Benjak<sup>1</sup>, E. Seliunin<sup>6</sup>, A. Shabbir<sup>47</sup>, A. Shalpegin<sup>23</sup>, S. Sharapov<sup>17</sup>, U. Sheikh<sup>23</sup>, A. Shevelev<sup>44</sup>, G. Sias<sup>19</sup>, M. Siccinio<sup>1</sup>, B. Sieglin<sup>1</sup>, A. Sigalov<sup>1</sup>, A. Silva<sup>6</sup>, C. Silva<sup>6</sup>, D. Silvagni<sup>1</sup>, J. Simpson<sup>17</sup>, S. Sipilä<sup>8</sup>, A. Snicker<sup>8</sup>, E. Solano<sup>57</sup>, C. Sommariva<sup>23</sup>, C. Sozzi<sup>7</sup>, M. Spacek<sup>1</sup>, G. Spizzo<sup>12</sup>, M. Spolaore<sup>12</sup>, A. Stegmeir<sup>1</sup>, M. Stejner<sup>43</sup>, D. Stieglitz<sup>1</sup>, J. Stober<sup>1</sup>, U. Stroth<sup>1,5</sup>, E. Strumberger<sup>1</sup>, G. Suarez Lopez<sup>4</sup>, W. Suttrop<sup>1</sup>, T. Szepesi<sup>28</sup>, B. Täl<sup>1</sup>, T. Tala<sup>38</sup>, G. Tardini<sup>1</sup>, M. Tardocchi<sup>7</sup>, D. Terranova<sup>12</sup>, M. Teschke<sup>1</sup>, E. Thorén<sup>35</sup>, W. Tierens<sup>1</sup>, D. Told<sup>1</sup>, W. Treutterer<sup>1</sup>, G. Trevisan<sup>12</sup>, M. Tripsky<sup>46</sup>, P. Ulbl<sup>1</sup>, G. Urbanczyk<sup>1</sup>, M. Usoltseva<sup>1</sup>, M. Valisa<sup>12</sup>, M. Valovic<sup>17</sup>, M. van Zeeland<sup>40</sup>, S. Vanmulders<sup>4</sup>, F. Vannini<sup>1</sup>, B. Vanovac<sup>10</sup>, P. Varela<sup>6</sup>, S. Varoutis<sup>31</sup>, T. Verdier<sup>43</sup>, G. Verdoolaege<sup>46,47</sup>, N. Vianello<sup>12</sup>, J. Vicente<sup>6</sup>, T. Vierle<sup>1</sup>, E. Viezzer<sup>27</sup>, G. Vogel<sup>1</sup>, I. Voitsekhovitch<sup>17</sup>, U. von Toussaint<sup>1</sup>, D. Wagner<sup>1</sup>, X. Wang<sup>1</sup>, M. Weiland<sup>1</sup>, D. Wendler<sup>1,5</sup>, A. E. White<sup>10</sup>, M. Willensdorfer<sup>1</sup>, B. Wiringer<sup>1</sup>, M. Wischmeier<sup>1</sup>, R. Wolf<sup>34</sup>, E. Wolfrum<sup>1</sup>, Q. Yang<sup>59</sup>, C. Yoo<sup>10</sup>, Q. Yu<sup>1</sup>, R. Zagorski<sup>22</sup>, I. Zammuto<sup>1</sup>, T. Zehetbauer<sup>1</sup>, W. Zhang<sup>59</sup>, W. Zholobenko<sup>1</sup>, M. Zilker<sup>1</sup>, B. Zimmermann<sup>1</sup>, A. Zito<sup>1</sup>, H. Zohm<sup>1</sup> & S. Zoletnik<sup>28</sup>

<sup>6</sup>Instituto de Plasmas e Fusão Nuclear, Instituto Superior Técnico, Universidade de Lisboa, Lisbon, Portugal. <sup>7</sup>ENEA, IFP-CNR, Milan, Italy. <sup>8</sup>Department of Applied Physics, Aalto University, Espoo, Finland. <sup>9</sup>Léonard de Vinci Pôle Universitaire Research Center, Paris, France. <sup>10</sup>MIT Plasma Science and Fusion Center, Cambridge, MA, USA. <sup>11</sup>Eindhoven University of Technology, Eindhoven, the Netherlands. <sup>12</sup>Consorzio RFX, Padova, Italy. <sup>13</sup>Princeton Plasma Physics Laboratory, Princeton, NJ, USA. <sup>14</sup>CEA/IRFM, Saint-Paul-lès-Durance, France. <sup>15</sup>Forschungszentrum Jülich, Jülich, Germany. <sup>16</sup>Institut Jean Lamour, Université de Lorraine, Nancy, France. <sup>17</sup>CCFE, Culham Science Centre, Abingdon, UK. <sup>18</sup>Aix-Marseille University, CNRS, Marseille, France. <sup>19</sup>Department of Electrical and Electronic Engineering, University of Cagliari, Cagliari, Italy. <sup>20</sup>ENEA, Centro Ricerche Frascati, Frascati, Italy. <sup>21</sup>ENEA, University of Milano-Bicocca, Milano, Italy. <sup>22</sup>Institute of Plasma Physics and Laser Microfusion, Warsaw, Poland. <sup>23</sup>Ecole Polytechnique Fédérale de Lausanne, Swiss Plasma Center, Lausanne, Switzerland. <sup>24</sup>ÖAW, IAP, University of Innsbruck, Innsbruck, Austria. <sup>25</sup>University of Wisconsin, Madison, WI, USA. <sup>26</sup>CFS, Fort Devens, MA, USA. <sup>27</sup>Universidad de Sevilla, Sevilla, Spain. <sup>28</sup>Centre for Energy Research, Budapest, Hungary. <sup>29</sup>York Plasma Institute, University of York, York, UK. <sup>30</sup>ENEA Consorzio CREATE, Naples, Italy. <sup>31</sup>Karlsruhe Institut für Technologie, Karlsruhe, Germany. <sup>32</sup>Institute of Plasma Physics, National Science Center Kharkov Institute of Physics and Technology, Krakov, Ukraine. <sup>33</sup>Institute of Plasma Physics of the CAS, Praha, Czech Republic. <sup>34</sup>Max-Planck-Institut für Plasmaphysik, Greifswald, Germany. <sup>35</sup>KTH Royal Institute of Technology, Stockholm, Sweden. <sup>36</sup>Barcelona Supercomputing Center, Barcelona, Spain. <sup>37</sup>Department of Physics, Durham University, Durham, UK. <sup>38</sup>VTT Technical Research Centre of Finland, Espoo, Finland. <sup>39</sup>ÖAW, IAP, Vienna University of Technology, Vienna, Austria. <sup>40</sup>General Atomics, San Diego, CA, USA. <sup>41</sup>Laboratoire de Physique des Plasmas, Ecole Polytechnique, Palaiseau, France. <sup>42</sup>ÖAW, Graz University of Technology, Graz, Austria. <sup>43</sup>Department of Physics, Technical University of Denmark, Lyngby, Denmark. <sup>44</sup>Ioffe Institute, St. Petersburg, Russian Federation. <sup>45</sup>Department of Physics, Chalmers University of Technology, Gothenburg, Sweden. <sup>46</sup>ERM/KMS, Brussels, Belgium. <sup>47</sup>Ghent University, Ghent, Belgium. <sup>48</sup>Electrical and Computer Engineering, University of California, Davis, CA, USA. <sup>49</sup>CREA, Barcelona, Spain. <sup>50</sup>Universität Greifswald, Greifswald, Germany. <sup>51</sup>ISC-CNR, Politecnico di Torino, Turin, Italy. <sup>52</sup>School of Physics, University College Cork, Cork, Ireland. <sup>53</sup>Technische Universität München, Garching, Germany. <sup>54</sup>Department of Industrial Engineering, University of Rome, Rome, Italy. <sup>55</sup>IGVP Universität Stuttgart, Stuttgart, Germany. <sup>56</sup>Budapest University of Technology and Economics, Budapest, Hungary. <sup>57</sup>Laboratorio Nacional de Fusión, CIEMAT, Madrid, Spain. <sup>58</sup>Università degli Studi della Tuscia, DEIM Department, Viterbo, Italy. <sup>59</sup>Chinese Academy of Sciences, Hefei, China.

## Methods

### ASDEX-Upgrade and discharge configuration

ASDEX-Upgrade is a medium-sized tokamak with a major radius of 1.65 m and a minor radius of 0.5 m. Plasma parameters for ELM suppression experiments are a toroidal magnetic field of  $B_T = 1.835$  T, plasma current of 898 kA and upper triangularity of 0.25. The plasma is externally heated by 2.3 MW of electron cyclotron resonance heating power and 6 MW of neutral beam injected heating power. In the ELM suppression case (discharge number #40180), no additional gas is injected after 2.6 s, whereas in the ELMing reference (#40180),  $2 \times 10^{21}$  deuterium particles per second are puffed to raise the density above the empirical upper boundary for ELM suppression<sup>9</sup>. In ASDEX-Upgrade, transient RMP fields are attenuated by eddy currents from nearby copper conductors. The axisymmetric position control system<sup>18,40</sup> causes periodic movements of the plasma boundary  $R_{\text{bnd}}^{\text{axi}}$ . These were measured and then compensated using a feed-forward trajectory of  $R_{\text{bnd}}^{\text{axi}}$  based on off-line equilibria from preceding but otherwise identical discharges (#39993 for ELMing and #40176 for ELM suppression). This compensation ensures a constant RMP field strength at the plasma surface throughout the rotation.

### Analysis of ECE data

The heterodyne radiometer at ASDEX-Upgrade measures ECE in the frequency range 78–105 GHz in experiments with  $B_T \approx 1.8$  T. The absolutely calibrated radiometer covers the edge region (73–89 GHz) with 36 channels having an intermediate frequency bandwidth of  $\Delta f_{\text{IF}} = 300$  MHz and a frequency spacing  $\delta f$  between 400 and 800 MHz.  $B_T$  was optimized to 1.835 T to have a channel spacing of  $\delta f = 400$  MHz in frequency, which corresponds to 5 mm in real space around the pedestal top. The sampling rate of the data acquisition system is 1 MHz. The ECE data were analysed from 3.3 s until 7.2 s for discharges #39993, #40180 and #40181 and until 6.8 s for #40176, due to loss of ELM suppression. ECE data affected by the ‘shine through’ have been filtered out by excluding the data in the local minimum of ( $T_{\text{rad}}$ ) and outside of it (Extended Data Fig. 1)<sup>35</sup>. Therefore, only ECE data in optically thick  $\tau > 3$  plasmas are included, where the measured  $T_{\text{rad}}$  approximates  $T_e$ , and has been tested against forward modelling<sup>35</sup> for single profiles (Extended Data Fig. 2). ELM-affected timepoints in ELMing plasma are discarded (Extended Data Fig. 3). In general, no radial shifts are applied to the ECE data.  $T_e$  contours from ECE are determined from 600 eV for ELM-suppressed and from 500 eV for ELMing plasma to 1.1 keV in 10 eV steps. Throughout the rotation, the density slightly increases and, thus,  $T_e$  decreases, but this has negligible impact on the outcome. The entire  $T_e$  profile is scaled by a linearly varying factor to account for the slight decrease in  $T_e$  throughout the analysed time windows. This multiplication factor is determined from ECE channels inside of the pedestal top and ranges from 0.9 to 1.1 for the case with the largest variation (#40181). Excluding this multiplication factor does not alter the conclusion and is reflected in the uncertainties.

Three methods to calculate the equilibrium are used to locate rational surfaces: (1) the axisymmetric equilibrium code Complete Interpretative Suit for Tokamak Equilibria (CLISTE)<sup>51</sup> evaluated at a single timepoint with hand-fitted profiles and no scrape-off layer currents; (2) CLISTE<sup>50</sup> with 1 ms time resolution and no kinetic constraints; and (3) the axisymmetric integrated data equilibrium (IDE)<sup>52</sup> code with 1 ms time resolution, kinetic constraints and current diffusion coupling assuming axisymmetric profiles<sup>53</sup>. The plasma boundary along the ECE measurement position is evaluated using (2) and (3), which also determines the range of measured magnetic surface perturbations, shown by coloured bands in Figs. 4 and 5b,e,h and Extended Data Fig. 4. IDE is used to illustrate positions of the rational surfaces as boxes in Figs. 3–5. The equilibrium data from (1) serves as input for the 3D MHD modelling. The normalized poloidal flux is defined as  $\Psi_N = \frac{\Psi - \Psi_{\text{lcs}}}{\Psi_{\text{mag}} - \Psi_{\text{lcs}}}$ , where  $\Psi_{\text{lcs}}$  is the poloidal flux at the last closed flux surface (lcs) and  $\Psi_{\text{mag}}$  at the magnetic axis.

For each ECE contour line, we use a least-squares fit minimization of simple trigonometric functions with the second harmonics and a linear function in time to account for possible drifts

$$f = \sum_{k=1,2} [a_k \sin(k\omega t) + b_k \cos(k\omega t)] + ct + d, \quad (2)$$

where  $\omega$  is  $2\pi f_{\text{RMP}}$  with  $f_{\text{RMP}} = 0.75$  Hz and  $t$  is the time. The analysed displacement of the  $n = 2$  component is then  $|\xi_{n=2}| = \sqrt{a_k^2 + b_k^2}|_{k=1}$  and the phase  $\phi_{n=2} = \arctan(b_k/a_k)|_{k=1}$ . These displacements are evaluated at the ECE measurement position and are very close to the nominal radial displacements, because the ECE diagnostic in ASDEX-Upgrade measures only 4 cm below the midplane. For the analysis to separate the ideal and resistive MHD contributions, we use  $\xi_{n=2}^{\text{3D}} = b_k|_{k=1} = |\xi_k| \sin(\phi_k)|_{k=1}$  and  $\xi_{n=2}^{\text{2D}} = a_k|_{k=1} = |\xi_k| \cos(\phi_k)|_{k=1}$ . The same procedure has been applied to the magnetic surface perturbations from VMEC at the ECE measurement position. The uncertainties are determined by the square root of the diagonal components from the covariance matrix of the residuals. Because of the large amount of data, these standard deviations are very small compared with the variation coming from the choice of equilibrium. Thus, the provided range of measured magnetic surface perturbations, indicated by the coloured bands in Figs. 4 and 5b,e,h and Extended Data Fig. 4, results from variations caused by the use of different equilibria for  $R_{\text{bnd}}^{\text{axi}}$ . The uncertainties of  $\delta\phi_{n=2}$  are estimated using error propagation of equation (1) assuming a standard deviation for the errors of the different analysis methods and the VMEC output. The island structure in Fig. 5 is revealed via  $\xi_{n=2}^{\text{2D}} - \xi_{n=2}^{\text{3D}} = |\delta\xi_{n=2}| \sin(\omega t + \delta\phi_{n=2})$  using

$$|\delta\xi_{n=2}| = \sqrt{(\xi_{n=2}^{\text{2D}} - \xi_{n=2}^{\text{3D}})^2 + (\xi_{n=2}^{\text{3D}} - \xi_{n=2}^{\text{kin}})^2} \text{ and equation (1).}$$

### MHD modelling

We use the 3D ideal MHD equilibrium code VMEC<sup>54</sup>, specifically the PARVMC version<sup>55</sup>. The 3D boundary from VMEC is often in good agreement with boundary measurements in ASDEX-Upgrade<sup>18,19,33,56</sup>. VMEC equilibria were calculated for two subsequent discharges #40180 and #40181 using axisymmetric CLISTE equilibria as input constrained by kinetic profiles without scrape-off layer currents (Extended Data Fig. 4). Magnetic data and kinetic profiles from Thomson scattering<sup>57</sup>, ECE and lithium beam diagnostic<sup>58</sup> were evaluated at 4.65 s within a time window of 100 ms, when the distortion in these profiles is close to its zero-crossing. The uncertainty in the input pressure profiles has been determined on the basis of the uncertainties derived from the mentioned diagnostics, as well as measurements of the effective charge used to calculate the ion density. We use 2,001 radial grid points, 4 toroidal mode numbers  $n_{\text{tor}}$  with 64 toroidal planes for one period and 32 poloidal mode numbers  $m_{\text{pol}}$ , and for #40181,  $m_{\text{pol}}$  was reduced to 26 to achieve reasonable convergence with  $f_{\text{col}} = 1 \times 10^{-11}$  and lower. Previous sensitivity studies have shown that this choice of parameters results in good agreement with measurements<sup>18</sup>. In the presented cases, the boundary displacements have been tested against boundary measurements using the helium beam diagnostic<sup>59</sup> (Extended Data Fig. 5). The radial resolution is crucial for identifying possible bump structures in the ideal MHD response, especially, in the case of an infernal mode<sup>60</sup>. For the ELM suppression case, very small changes ( $< 0.1$  mm) in the displacement amplitude around the 7/2 is observed between 511, 1,501 and 2,001 radial grid points equidistant in toroidal magnetic flux, indicating sufficient radial resolution. Effective currents for the RMP coils were used to account for the attenuation by nearby conducting material. The attenuation is calculated using the finite element methods and applied to the coil current resulting in an effective RMP coil current (Fig. 2a).

The resistive MHD modelling has been conducted using the non-linear extended MHD code JOREK coupled with free boundary extension STARWALL<sup>44</sup> in realistic tokamak geometry using a reduced MHD model with extensions for self-consistent bootstrap current evolution, two-fluid diamagnetic effects and neoclassical friction. Transport

coefficient profiles are adjusted to keep kinetic profiles stationary. Viscosity  $\nu$  is realistic with  $1 \text{ m}^2 \text{ s}^{-1}$  in the pedestal region. The main assumption made is equating ion temperature to  $T_e$ , which is reasonable because they differ by about 20% in plasmas with ELM suppression. JOREK simulations use the axisymmetric CLISTE equilibrium from the ELM suppression case (#40180), the experimental RMP coil currents and the experimental kinetic profiles as for VMEC.

### Data availability

Raw data were generated by the ASDEX-Upgrade Team. Further data that support the findings of this study are available from the corresponding author upon reasonable request. Source data are provided with this paper.

### Code availability

The PARVMC code is available via GitHub at <https://github.com/ORNL-Fusion/PARVMC.git>. The JOREK code is available upon reasonable request to [admin@jorek.eu](mailto:admin@jorek.eu) (<https://www.jorek.eu>).

### References

51. McCarthy, P. J. Identification of edge-localized moments of the current density profile in a tokamak equilibrium from external magnetic measurements. *Plasma Phys. Control. Fusion* **54**, 015010 (2012).
52. Fischer, R. et al. Estimation and uncertainties of profiles and equilibria for fusion modeling codes. *Fusion Sci. Technol.* **76**, 879–893 (2020).
53. Fischer, R., Fuchs, C., Kurzan, B. & Suttrop, W. Integrated data analysis of profile diagnostics at ASDEX Upgrade. *Fusion Sci. Technol.* **58**, 675–684 (2010).
54. Hirshman, S. P. Steepest-descent moment method for three-dimensional magnetohydrodynamic equilibria. *Phys. Fluids* **26**, 3553–3568 (1983).
55. Seal, S. K. et al. Parallel reconstruction of three dimensional magnetohydrodynamic equilibria in plasma confinement devices. In *46th International Conference on Parallel Processing (ICPP)* 282–291 (IEEE, 2017); <https://doi.org/10.1109/ICPP.2017.37>
56. Suárez-López, G. et al. Validation of high-fidelity ion cyclotron range of frequencies antenna coupling simulations in full 3D geometry against experiments in the ASDEX Upgrade tokamak. *Plasma Phys. Control. Fusion* **62**, 125021 (2020).
57. Kurzan, B. & Murmann, H. D. Edge and core Thomson scattering systems and their calibration on the ASDEX Upgrade tokamak. *Rev. Sci. Instrum.* **82**, 103501 (2011).
58. Willensdorfer, M. et al. Characterization of the Li-BES at ASDEX Upgrade. *Plasma Phys. Control. Fusion* **56**, 025008 (2014).
59. Griener, M. et al. Helium line ratio spectroscopy for high spatiotemporal resolution plasma edge profile measurements at ASDEX Upgrade (invited). *Rev. Sci. Instrum.* **89**, 10D102 (2018).
60. Dong, G. Q. et al. Stability of ideal and non-ideal edge localized infernal mode. *Phys. Plasma* **24**, 112510 (2017).
61. Schneider, P. A. et al. Differences in the H-mode pedestal width of temperature and density. *Plasma Phys. Control. Fusion* **54**, 105009 (2012).

### Acknowledgements

We are grateful to C. Paz-Soldan, E. Poli, Q. Yu and H. Zohm for fruitful discussions. This material is based upon work supported by the US Department of Energy under award DE-SC0021968. This work has been carried out within the framework of the EUROfusion Consortium, funded by the European Union via the Euratom Research and Training Programme (grant agreement no. 101052200-EUROfusion). Views and opinions expressed are, however, those of the author(s) only and do not necessarily reflect those of the European Union or the European Commission. Neither the European Union nor the European Commission can be held responsible for them.

### Author contributions

M.W. led the analysis and experiments, and wrote sections. V.M. provided JOREK simulations. M.H. supported JOREK simulations and wrote sections. W.S. programmed RMP coils and discharges, and executed experiments. M.C. provided support for PARVMC within the stellopt suite. M.D. provided CLISTE equilibrium reconstruction. R.F. provided IDE equilibrium reconstruction. N.L. participated in initial experiments and analysis. J.P. provided equilibria for uncertainty analysis. O.S. supported the ECE operation and calibration. G.S.L. provided software to carry out and analyse the PARVMC simulations. D.W. supported the helium beam operation and data analysis. The ASDEX Upgrade Team provided the experimental infrastructure.

### Funding

Open access funding provided by Max Planck Society.

### Competing interests

The authors declare no competing interests.

### Additional information

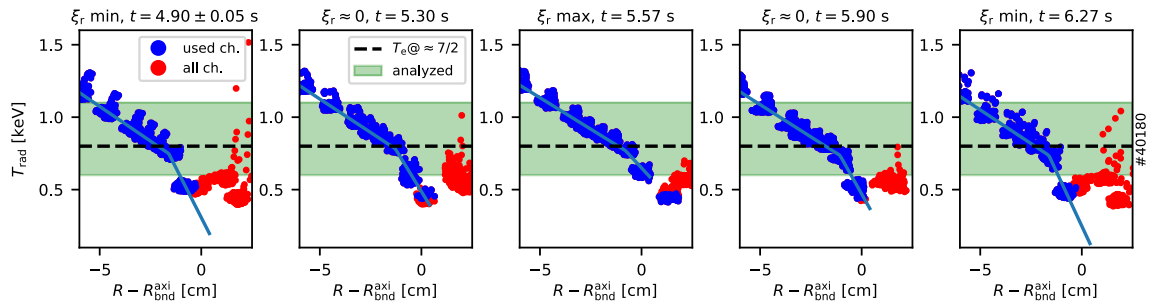
**Extended data** is available for this paper at <https://doi.org/10.1038/s41567-024-02666-y>.

**Supplementary information** The online version contains supplementary material available at <https://doi.org/10.1038/s41567-024-02666-y>.

**Correspondence and requests for materials** should be addressed to Matthias Willensdorfer.

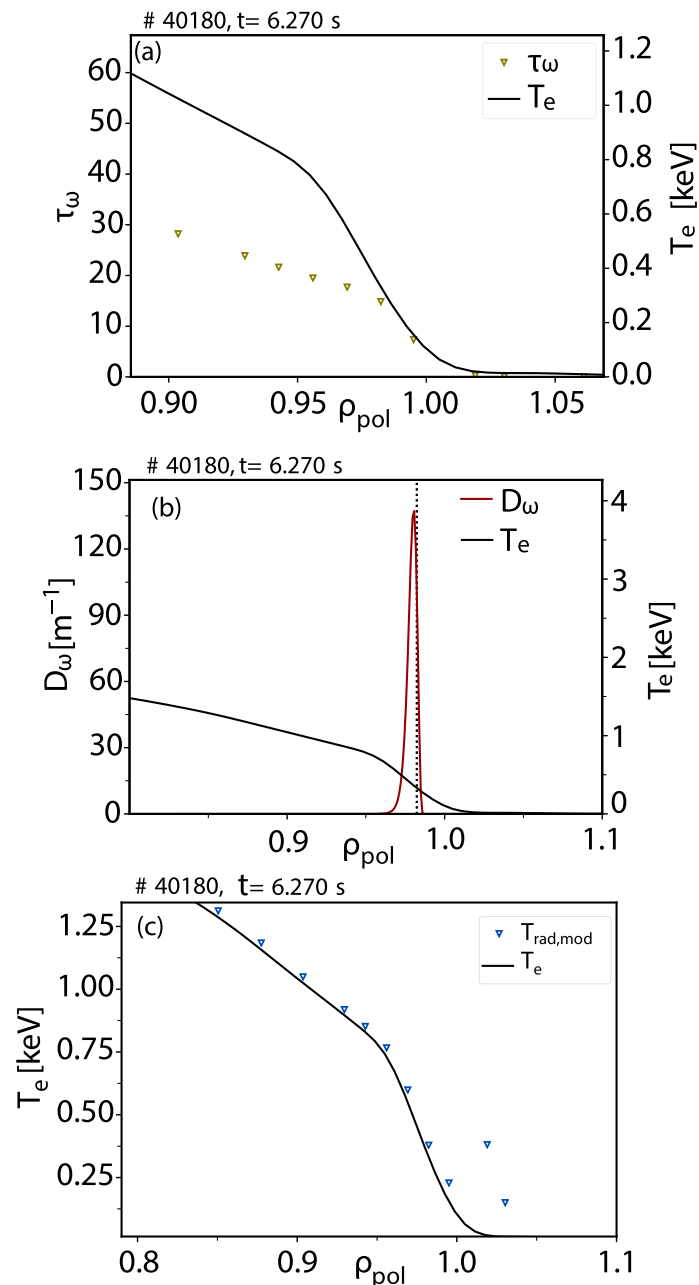
**Peer review information** *Nature Physics* thanks Richard Fitzpatrick and Guosheng Xu for their contribution to the peer review of this work.

**Reprints and permissions information** is available at [www.nature.com/reprints](http://www.nature.com/reprints).



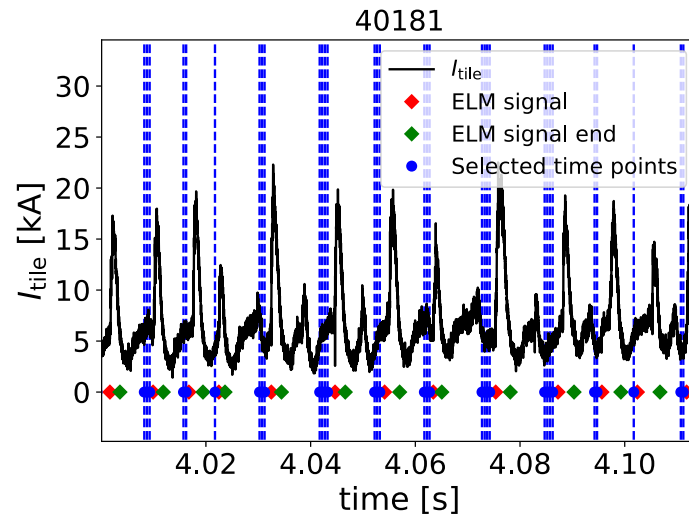
**Extended Data Fig. 1 | Measured profiles from the electron cyclotron emission.** Radiation temperature ( $T_{\text{rad}}$ ) by the electron cyclotron emission diagnostic versus  $R$  at the measurement position relative to the axisymmetric plasma boundary  $R_{\text{bnd}}^{\text{axi}}$ . Shown profiles are from certain phases of the rotation indicated by the displacement  $\xi_r$  and the time  $t$ . Channels outside the local

minimum and channels with zero or positive gradients are discarded (red) and whereas the others (blue) are included. Contours in ELM suppression are evaluated from 0.6 to 1.1 keV on (green area) and the horizontal dashed line shows the electron temperature  $T$  level roughly at the  $7/2$  rational surface surface ( $T_{@ \approx 7/2}$ ). A two-line fit<sup>61</sup> (blue line) is used to illustrate the pedestal top.



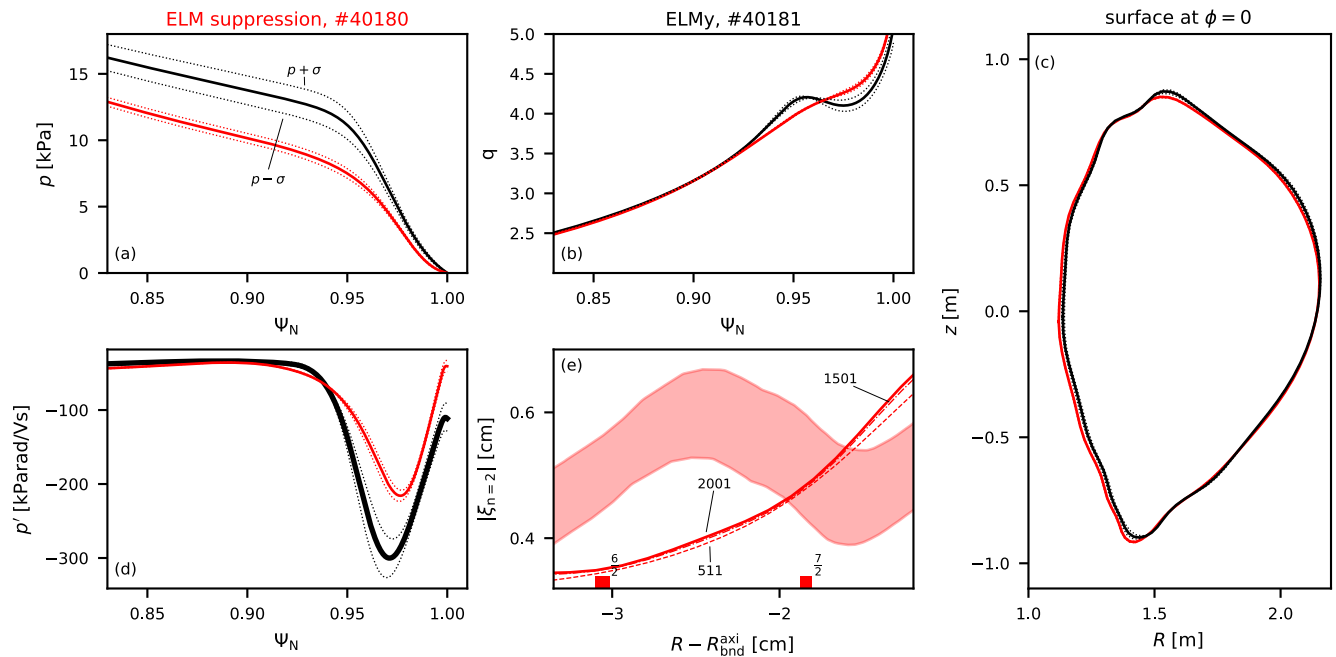
**Extended Data Fig. 2 | Forward modelling of the electron cyclotron transport.** The electron cyclotron transport has been exemplarily modelled for one representative time point  $t = 6.270$  s of discharge #40180 assuming axisymmetric equilibrium and profiles<sup>35</sup>. Profiles using the square root of the normalised poloidal flux  $\rho_{\text{pol}}$  of the (a) optical thickness ( $\tau_\omega$ ) of channels with frequency  $\omega$  from the electron cyclotron emission (ECE) diagnostic and the given electron temperature  $T_e$  profile. In the region of interest, which is the pedestal

top, the optical depth is thick ( $\tau_\omega \approx 20$ ,  $\tau_\omega \approx 3$  is considered to be optical thick). (b) shows the origin of the observed intensity ( $D_\omega$ ), which is close to cold resonance frequency (vertical dotted line) and  $T_e$  at the second y-axis. (c) Comparison between the modelled radiation temperature  $T_{\text{rad,mod}}$  from a synthetic ECE diagnostic in comparison to the given  $T_e$ . In optical thick plasmas, the  $T_{\text{rad}}$  is a good proxy for  $T_e$ .



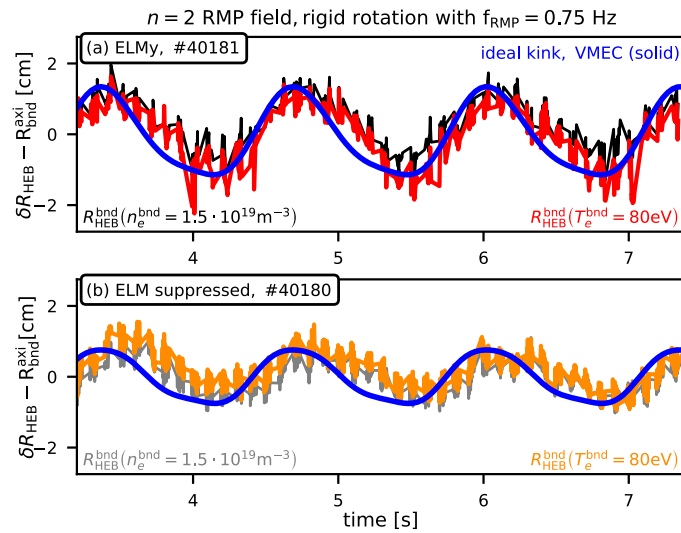
**Extended Data Fig. 3 | Identifying timing of edge-localised modes.** Timetraces of shunt current measurements from a tile  $I_{\text{tile}}$  to identify the timing of edge-localised modes (ELMs) in discharge #40181. Representative examples of selected time points for the electron cyclotron emission diagnostic before the

ELM onsets (red diamonds) are shown as vertical dashed blue lines. Because of the high temporal resolution several clustered time points appear as one thick line.



**Extended Data Fig. 4 | Equilibrium properties from discharge #40180 and #40181.** (a) Input pressure profiles versus normalised poloidal flux ( $\Psi_N$ ) for the VMEC and JOREK code from edge-localised mode (ELM) suppression (red) and ELMy (black) plasmas are shown. Panel (a) shows the used pressure profile (solid) plus and minus standard deviation  $\sigma$  (thin dashed lines) from the pressure profile  $p$  measurements at the pedestal top, which is roughly 5% and 10% for the ELM suppression (red) and ELMy case (black), respectively. Same for panel (b) showing safety factor  $q$  profile, (c) poloidal cut at the toroidal angle ( $\phi = 0$ ) using the vertical coordinate  $z$  versus the radial coordinate  $R$  from the corrugated last closed flux surfaces from the VMEC code and (d) the pressure gradient profiles using  $p' = \frac{\partial p}{\partial \Psi_N}$  with their impact from the pressure profile uncertainties. Panel

(e) shows measured displacement amplitude  $|\xi_{n=2}|$  with toroidal symmetry of  $n = 2$  versus  $R$  at the measurement position relative to the axisymmetric plasma boundary  $R_{\text{bnd}}^{\text{axi}}$ . The band indicates the range resulting from different equilibrium reconstruction methods (see Methods section). The corresponding displacement amplitudes from the VMEC code for discharge #40180 (ELM suppression case) with different radial resolution are added using 511 (dashed), 1501 (dashed-dotted) and 2001 (solid) flux surfaces. The displacement amplitudes from VMEC at the measurement position barely change from 511 to 2001 flux surfaces between the 6/2 and 7/2 rational surface showing sufficient radial resolution.



**Extended Data Fig. 5 | Comparison between measured boundary displacements and ideal MHD.** Displacement measurements using the helium beam (HEB)<sup>58</sup> diagnostic  $R_{\text{HEB}}^{\text{bnd}}$  at the radial coordinate  $\delta R_{\text{HEB}}$  relative to the axisymmetric plasma boundary  $R_{\text{bnd}}^{\text{axi}}$  using Iso- electron temperature  $T_e^{\text{bnd}}$  (red) and - electron density  $n_e^{\text{bnd}}$  (black) at the boundary during (a) a plasma with edge localised modes (ELMs), discharge #40181, and (b) one with ELM-suppression

#40180 using  $T_e^{\text{bnd}}$  (orange) and  $n_e^{\text{bnd}}$  (grey). The RMP field with toroidal mode number  $n = 2$  rotates with a frequency  $f_{\text{RMP}}$  of 0.75 Hz. Measurements are compared to ideal MHD predictions using VMEC (solid blue). Measured and calculated boundary displacement are in good agreement. The ELMy case has lower distortion amplitude due to smaller pressure gradients.